ACS Sustainable Chemistry & Engineering

Research Article

pubs.acs.org/journal/ascecg

Acidolysis of α-O-4 Aryl-Ether Bonds in Lignin Model Compounds: A Modeling and Experimental Study

Adam W. Pelzer,*[,⊥] Matthew R. Sturgeon,[†,‡] Abraham J. Yanez,[⊥] Gina Chupka,[†,‡] Marykate H. O'Brien,[†,‡] Rui Katahira,[†,‡] Randy D. Cortright,[§] Liz Woods,[§] Gregg T. Beckham,*[,†,‡] and Linda J. Broadbelt*[,⊥]

[†]National Advanced Biofuels Consortium, National Renewable Energy Laboratory, Golden, Colorado 80401, United States

[‡]National Bioenergy Center, National Renewable Energy Laboratory, Golden, Colorado 80401, United States

[§]Virent, Inc., Madison, Wisconsin 53704, United States

[⊥]Department of Chemical and Biological Engineering, Northwestern University, Evanston Illinois 60208, United States

Supporting Information

ABSTRACT: Lignocellulosic biomass offers a vast, renewable resource for the sustainable production of fuels and chemicals. To date, a commonly employed approach to depolymerize the polysaccharides in plant cell walls employs mineral acids, and upgrading strategies for the resulting sugars are under intense development. Although the behavior of cellulose and hemicellulose is reasonably well characterized, a more thorough understanding of lignin depolymerization mechanisms in acid environments is necessary to predict the fate of lignin under such conditions and ultimately to potentially make lignin a viable feedstock. To this end, dilute acid hydrolysis experiments were performed on two lignin model compounds containing the α-O-4 ether linkage at two temperatures concomitant with dilute acid pretreatment. Both primary and secondary products were tracked over time, giving insight into the reaction kinetics. The only difference between the two model compounds was the presence or absence of a methyl group on the α-carbon, with the former being typical of native lignin. It was found that methylation of the α-carbon increases the rate of reaction by an order of magnitude. Density functional theory calculations were performed on a proposed mechanism initiated by a nucleophilic attack on the α-carbon by water with a commensurate protonation of the ether oxygen. The values for the thermodynamics and kinetics derived from these calculations were used as the basis for a microkinetic model of the reaction. Results from this model are in good agreement with the experimental kinetic data for both lignin model compounds and provide useful insight into the primary pathways of α-O-4 scission reactions in acid-catalyzed lignin depolymerization. The distribution of primary and secondary products is interpreted as a function of two barriers of formation exhibiting opposite trends upon methylation of the α-carbon (one barrier is lowered while the other is increased). Such insights will be needed to construct a comprehensive model of how lignin behaves in a common deconstruction approach.

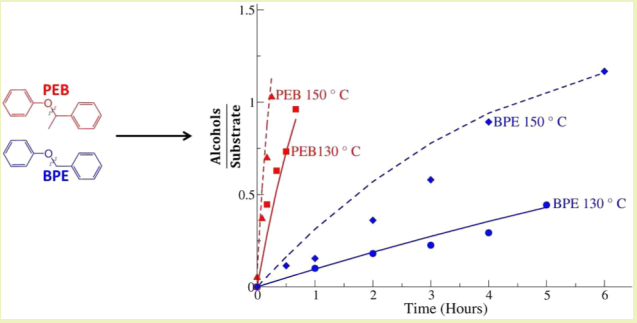

KEYWORDS: *Density functional theory, Microkinetic modeling, α-O-4, Ether bond*

INTRODUCTION

Two key polymers in plant biomass, cellulose and hemicellulose, can be depolymerized and converted into ethanol or upgraded to hydrocarbon fuels or other useful organic chemicals by either biological or chemical/thermochemical means using established methods.[1−6] Efforts to find cost effective ways to valorize lignin, the third polymer found in biomass, have been less successful to date[7−9] and have led to attempts to genetically engineer feedstocks with lower levels of lignin.[10−12] However, some amount of lignin will always be necessary in order to maintain the structural integrity of plant cells, and lignin has the potential to produce an array of valuable compounds, aside from its potential as a biofuel feedstock.[13−17] The ability to cost effectively valorize lignin, rather than burning it for heat and power, would be an important step forward to improve the economic viability of the biorefinery.[18,19]

Important initial investigations on the depolymerization of native lignin and analysis of the product distributions were performed by Lunquist and coworkers using dilute acid and dioxin-water.[13,17−20] An analogous method to depolymerize lignin into smaller, more usable compounds is dilute acid-catalyzed hydrolysis (1−2 wt % acid loading). This has been found to be effective at breaking down lignin under moderate temperatures and relatively modest times (120−180 °C and as short as 1 min),[21] leading to reduced molecular weight compounds like monoaromatic alcohols.[22,23] However, upon

Received: January 28, 2015
Revised: March 19, 2015
Published: April 22, 2015

DOI: 10.1021/acssuschemeng.5b00070
ACS Sustainable Chem. Eng. 2015, 3, 1339−1347

cooling, it has been found that some of the monomers react to form new carbon−carbon bonds, thus leading to even more recalcitrant products than the original compound. In addition, each separate linkage type will have its own mechanism and product distribution leading to a complex final mixture of compounds. These secondary products reduce the yield of low molecular weight species from lignin and can potentially poison downstream chemical or biological catalysts. Understanding and predicting the proportions of these two types of products are essential in optimizing reaction conditions that most effectively depolymerize lignin. A complicating factor is that although cellulose and hemicellulose are composed of five and six carbon sugars linked by ether bonds, lignin is a random copolymer composed of three phenolic monomers linked by a range of different bond types.[24−28] These linkages can be classified into two general types: a range of ether bonds where monomers are linked via an oxygen atom, and carbon−carbon bonds where monomers are joined to one another at various points on the phenol rings. One of the simpler ether linkages in lignin is the α-O-4 aryl-ether linkage, which can constitute up to 15% of the total linkages[29] depending on the source of biomass, although the typical literature value for woody biomass is 6−8%.[27,30] More recent 2D NMR experiments find them to be as low as 0.3% of all linkages and attribute higher values to mislabeling of peaks in previous spectra.[20,27] Regardless of the exact value, the investigation of such compounds is relevant to the processing of native lignin as the formation of carbon−carbon bonds from monomeric species leads to the formation of more recalcitrant species than the original substrate. Understanding the mechanistic source of these products and how to optimize processes to limit their formation is an important challenge.

The use of native lignin in both experimental and modeling studies is problematic because the product distribution and chemical reaction network of acidolysis on the full lignin polymer are extremely complex. Therefore, it is instructive to focus on lignin model compounds with only a single representative linkage type to simplify the overall reaction into the most basic relevant units.[31,32] The coupling of experimental investigations of well-defined model compounds with detailed kinetic calculations such as microkinetic modeling has proven a successful method for gaining understanding of reaction mechanisms.[33−36] Microkinetic modeling is a framework that quantitatively describes a reacting system in terms of a chemical reaction network based upon elementary steps without making an assumption about the rate-limiting step. The model tracks all relevant chemical intermediates that are involved in the pathways guiding reactants to products. Quantum chemical calculations are often an important companion to microkinetic modeling studies, as they are able to provide thermodynamic and kinetic parameters for the elementary steps that comprise the postulated mechanism on which the microkinetic model is based.[37−40] Microkinetic models have become an important tool and are applied to problems ranging from heterogeneous catalysis to gas-phase combustion, but no published microkinetic model exists for lignin model compound acidolysis. A major strength of microkinetic modeling is that because of its sound physical and chemical basis, it is applicable over a wide range of conditions, thus aiding in efforts to identify reaction conditions that maximize a quantity of interest.[41−45]

In this study, two α-O-4 model compounds, benzylphenyl ether (BPE) and 1-(phenoxyethyl)benzene (PEB) (Figure 1),

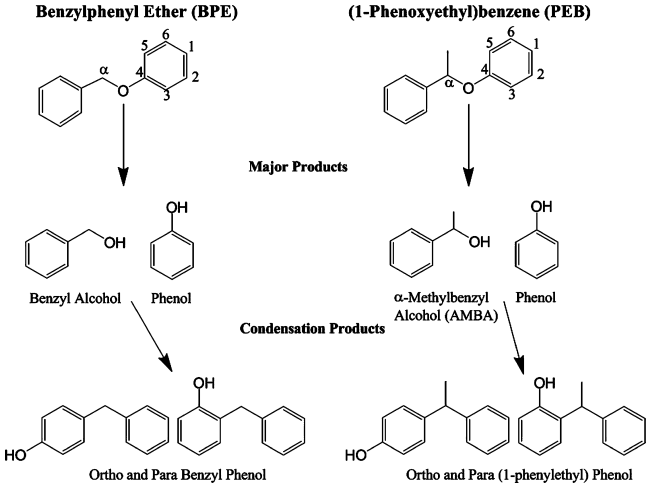

Figure 1. α-O-4 model compounds with major and condensation products.

were synthesized and subjected to dilute acid hydrolysis at temperatures and acid loadings similar to those used in dilute acid pretreatment. BPE is an aryl alkyl ether containing the α-O-4 bond and has been a popular choice in model studies focused on reactions of lignin, coal, and kerogen. These previous studies have investigated BPE breakdown at a range of temperatures and conditions.[15,16,30,46−51] The usefulness of this compound is due to its simplicity; the effects of various substituents can be determined independently by comparing them to the most elementary case.

PEB is a comparable model compound to BPE and allows us to isolate the effect of methylation on the α-carbon. This more accurately mimics native lignin where β- and γ-carbons are present. Loss of the substrate and appearance of the primary and secondary condensation products were measured over time. A quantum chemical model based on density functional theory (DFT) and microkinetic modeling based on a proposed mechanism involving nucleophilic attack on the α-carbon (Figure 2) were applied, and the results were compared to the experimental data. An alternative mechanism involving the protonation of the ether oxygen and the creation of a free benzyl cation was also investigated, as a number of schemes have been proposed to model ether acidolysis.[52−54] However, the nature of the benzyl cation involving an undelocalized charge on a primary carbon[55] along with results from preliminary calculations ruled this mechanism out. Previous quantum chemical calculations utilizing this mechanism without explicit solvent were found to underestimate C−O bond scission barriers.[47] No microkinetic model was investigated, but the associated potential energy surface indicates an overestimation of condensation product formation.

Lastly, we note that native lignin contains hydroxyl and methoxyl substituents, which are not included in the model compounds used here. The effects of these substituents have recently been studied in the case of β-O-4 linkages,[32] and theoretical investigation of the effects in α-O-4 compounds will be performed in the future.

EXPERIMENTAL SECTION

Synthesis and Acidolysis of Model Compounds. Benzyl phenyl ether, BPE, was synthesized according to the following method: 5 mL of benzyl bromide (33 mmol), phenol (3.1023 g, 33 mmol), K_2CO_3 (8.29 g, 60 mmol), and KI (0.8295 g, 5 mmol) were

DOI: 10.1021/acssuschemeng.5b00070
ACS Sustainable Chem. Eng. 2015, 3, 1339−1347

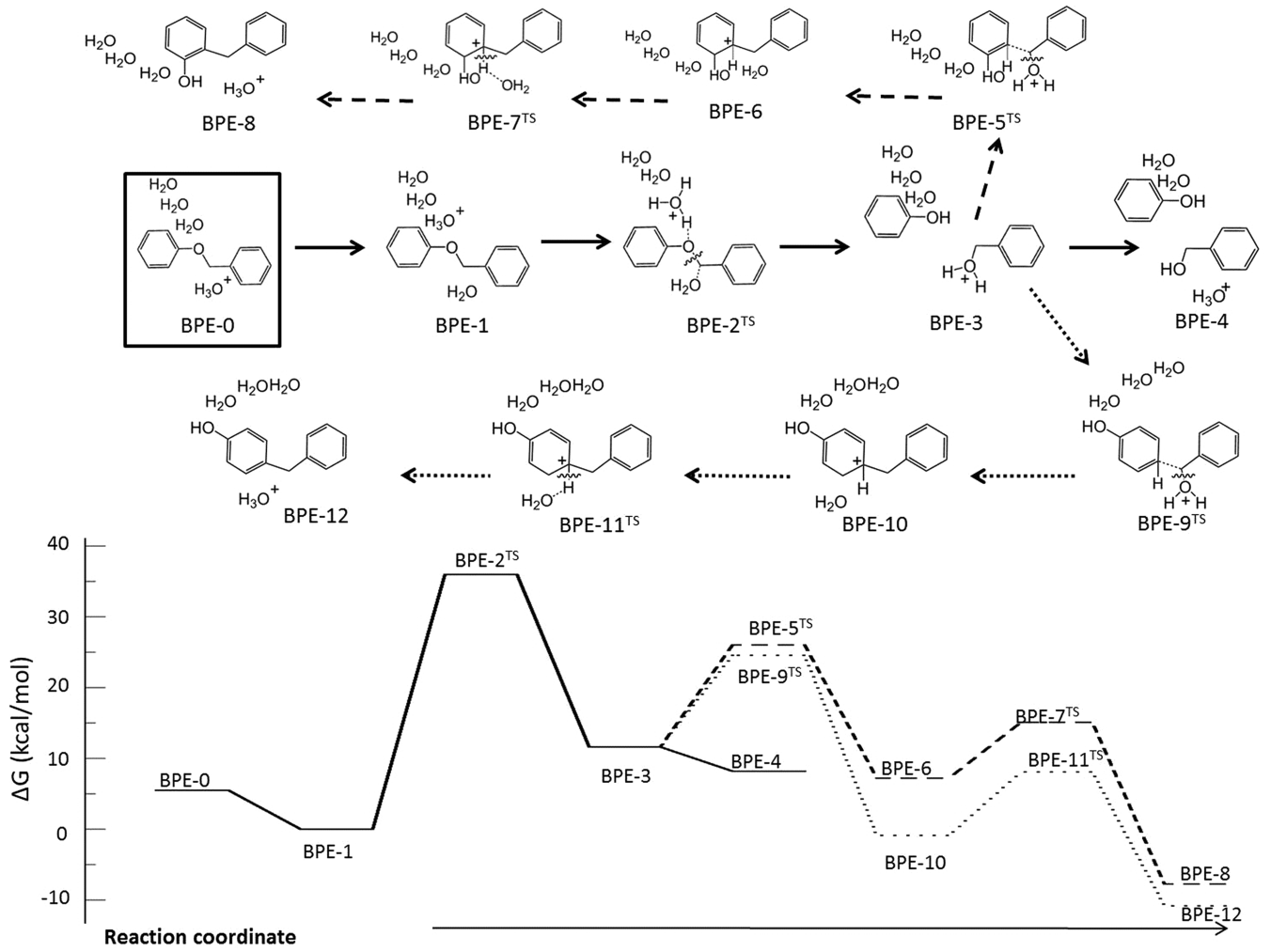

Figure 2. Reaction coordinate for the formation of the major products (solid line) along with the ortho (---) and para (····) condensation products for the BPE system. Note that the line scheme used in the plot is maintained in the arrow scheme between the corresponding structures. These arrows are only a guide for the eye. See SI-Figure 1 and SI-Figure 2 in the Supporting Information for corresponding three-dimensional structures.

charged into a round-bottomed flask equipped with a reflux condenser. The mixture was heated to reflux in 45 mL acetone and stirred overnight. The mixture was filtered and the resultant solution concentrated *in vacuo*. Deionized water (50 mL) was added. The reaction mixture was extracted with ethyl acetate (25 mL) three times. The combined ethyl acetate was washed with a brine solution, dried over $MgSO_4$, and filtered. The solution was concentrated *in vacuo*, and BPE was crystallized from a cold ethanol solution and obtained as a white solid (84% yield). NMR matched commercially available samples (Aldrich).

1-(Phenoxyethyl)benzene, PEB, was synthesized according to the following method: phenol (1.2 g, 12.7 mmol), K_2CO_3 (2.10 g, 15.2 mol), KI (0.40 g), and (1-bromoethyl)benzene (2.36 g, 10.6 mmol) were charged into a round-bottomed flask equipped with a reflux condenser and dissolved in 25 mL acetone. The mixture was heated to reflux with stirring overnight. The solution was filtrated and concentrated *in vacuo*. The resultant oil was dissolved in 50 mL ethyl acetate, and deionized water (60 mL) was added. The mixture was extracted with ethyl acetate (50 mL) three times. The combined organic extracts were washed with a brine solution, dried over $MgSO_4$, and filtered. Ethyl acetate was removed *in vacuo* to give a slightly yellow oil that was purified by silica gel column chromatography developed with *n*-hexane:ethyl acetate (40:1) to obtain a white crystalline solid (68% yield). m/z = 198.01.

All acidolysis experiments were conducted in 0.2 M H_2SO_4 at a concentration of 0.016 M substrate. To minimize experimental error, a stock solution of each substrate dissolved in acetone was used to deliver a known amount of substrate (0.08 mmol in BPE and 0.075 mmol in PEB) into reaction vessels. One milliliter of the stock solution was pipetted into different reaction vials. The solutions were carefully dried under a stream of N_2. Stir bars and 5 mL of 0.2 M H_2SO_4 were then added to each vial. The vials were sealed with a Teflon cap equipped with a Viton O-ring, placed into a preheated stirring heating block at 130 or 150 °C, and stirred with heating throughout the experiment. After prescribed reaction times, each vial was removed from the block and cooled by submersion into room temperature water. Once cool, 5 mL of acetone was added to each vial along with enough sodium bicarbonate to neutralize the acid. In each case, gas chromatography−mass spectrometry (GC/MS) analysis was strictly used for component identification only. Samples were prepared by taking a 1 mL aliquot of solution and performing a liquid/liquid extraction with 1 mL of methylene chloride. The methylene chloride layer was used for GC analysis. For quantitative analysis, a 1 mL aliquot was removed for high-performance liquid chromatography (HPLC) analysis.

Quantum Chemical Model. All calculations were performed using the Gaussian 09 software package.[56] Geometry optimizations were performed at the default levels for force constants and SCF convergence using the 6-311++g** basis set. Saddle points were found by performing constrained optimizations along a proposed reaction coordinate. Transition states were verified using frequency calculations, and when imaginary frequencies were produced, the degree of freedom was examined visually to ensure that it corresponded to the proper reaction coordinate. Intrinsic reaction coordinate calculations

DOI: 10.1021/acssuschemeng.5b00070
ACS Sustainable Chem. Eng. 2015, 3, 1339−1347

Table 1. Activation Energies (E_a) and Pre-exponential Factors (A) for the BPE Microkinetic Model[a]

reaction	$A_{forward}$ (L/mol·s)	$E_{a\text{-}forward}$ (kcal/mol)	$A_{reverse}$ (L/mol·s)	$E_{a\text{-}reverse}$ (kcal/mol)
BPE-0 ⇆ BPE-1	5.2×10^{10}	0	1.4×10^{10}	4.8
BPE-1 ⇆ BPE-3	1.2×10^{5}	23.3 (**21.5 ± 0.097**)	1.0×10^{5}	11.4 (**9.6 ± 0.097**)
BPE-3 ⇆ BPE-4	5.2×10^{10}	0	3.6×10^{8}	0.7
BPE-3 ⇆ BPE-6	2.7×10^{6}	7.0 (**8.1 ± 0.61**)	6.4×10^{12}	19.2 (**20.3 ± 0.61**)
BPE-6 ⇆ BPE-8	3.5×10^{10}	3.5	3.3×10^{11}	20.2
BPE-3 ⇆ BPE-10	6.2×10^{5}	8.5 (**7.9 ± 0.61**)	6.1×10^{10}	25.1 (**24.5 ± 0.61**)
BPE-10 ⇆ BPE-12	1.6×10^{9}	2.1	5.9×10^{10}	15.0

[a]Values in bold indicate 95% probability intervals obtained through parameter optimization. See text for details.

were also performed to ensure that the saddle point was a true transition state between the appropriate reactants and products.

Because water is a key reactant in our proposed mechanism, we apply a hybrid cluster-continuum solvation model.[57] An investigation into the proper functional and necessary number of explicit water molecules was performed to determine which combination gave the most accurate description of the system based on experimental values for the pK_a of protonated ethers.[58,59] On the basis of these results, the OLYP functional[60] was chosen for all calculations discussed below. Three waters were found to be the optimal number to solvate properly the proton. See the Supporting Information for further details.

Mickrokinetic Model. The kinetics and thermodynamics predicted based on the quantum chemical model developed in the previous section were used to model the reaction kinetics at all temperatures via microkinetic modeling, and the predicted concentration profiles were compared to the experimental ones. Using the rigid-rotor and harmonic oscillator approximations, the standard statistical-mechanical formulas were evaluated to obtain estimates of the Gibbs free energy of activation ($\Delta G^{\ddagger}$) for each elementary step. The thermodynamic reference state is 1 M. Rate constants were calculated over a range of 1000 K using the Eyring formulation[61] of transition-state theory (TST) with the transmission coefficient κ set to unity (eq 1). Arrhenius plots were then constructed, and the frequency factor A and activation energy E_a were obtained for each elementary step

$$k_{TST} = \kappa \frac{k_B T}{h} e^{-\Delta G^{\ddagger}/RT} \quad (1)$$

where k_{TST} is the rate constant for that elementary step, k_B is Boltzman's constant, h is Planck's constant, R is the gas constant, T is the temperature, and $\Delta G^{\ddagger}$ is the Gibbs free energy of activation.

Barrierless reactions such as proton diffusion in solvent and acid/base equilibria were assigned forward activation energies of 0. Frequency factors in the thermodynamically favorable direction (i.e., having $\Delta G_{rxn} < 0$) were estimated using the Smoluchowski diffusion-limited rate constant[62]

$$k_{diffusion} = \frac{8 k_B T}{3\eta}$$

where $k_{diffusion}$ is the diffusion-limited rate constant and η is the viscosity.

The activation energies and frequency factors for the reverse direction are calculated by applying the equilibrium constraint

$$K_{eq}(T) = e^{-\Delta G_{rxn}/RT} \rightarrow A^{rev} e^{-E_a^{rev}/RT} = \frac{k_{diffusion}}{K_{eq}(T)}$$

where K_{eq} is the equilibrium constant and A^{rev} and E_a^{rev} are the frequency factor and activation energy for the reverse reaction, respectively.

The microkinetic model was derived by coupling the design equations of an ideal batch reactor with the net rate expressions for each species, resulting in a system of ordinary differential equations (ODEs) governing the time evolution in molar concentration of each species considered. The ODEs were numerically solved using DDASAC as a function of the experimentally defined initial conditions of temperature, initial substrate concentration, and proton loading (by noting that one equivalent of sulfuric acid yields two proton equivalents). The temperature in all simulations was defined to be constant, in accordance with the reported experimental procedure. The solution of these ODEs results in the concentration profiles as a function of time for all species considered in the microkinetic model.

RESULTS AND DISCUSSION

Acidolysis of Benzylphenyl Ether (BPE). The raw data for the acidolysis experiments on BPE are given in the Supporting Information. The major products of acid cleavage (phenol and benzyl alcohol) are in a ratio of approximately one to one at all temperatures. The ratio of major products to the total condensation products is approximately four to one at all temperatures. The mass balances reported in the Supporting Information (SI-Table 1) indicate that some material is lost during reaction; charring (a known issue at these reaction temperatures in acidic conditions)[32] was visually observed. Changes in the ortho/para ratio of the condensation products over time imply that either the ortho or para isomers (or both) are taking part in further chemical reactions rather than simply accruing, leading to higher molecular weight condensation species that were observed as charring but not quantitatively measured.

As discussed above, the BPE system was modeled with four explicit water molecules and a proton, with one of the four waters being used in a nucleophilic attack and three used to solvate the proton. The reaction coordinate leading to the formation of the major and condensation products is shown in Figure 2, and the three-dimensional structures are shown in the Supporting Information.

Structure BPE-0 represents the substrate without a proton in the solvent near the ether oxygen, whereas structure BPE-1 has the proton in a position to protonate the ether oxygen. The initial step in the reaction is proposed to be a concerted process with a nucleophilic attack on the α-carbon by a water molecule commensurate with the localization of the proton from the solvent on the ether oxygen (structure BPE-2^{TS}). The result of this attack is a mixture of solvated phenol and protonated benzyl alcohol (structure BPE-3). The deprotonation of the protonated benzyl alcohol leads to the formation of the second major product (structure BPE-4).

The condensation products are formed by the addition of the protonated benzyl alcohol at the ortho or para positions of phenol (structures BPE-5^{TS} and BPE-9^{TS}) leading to the release of a water molecule. These structures are then deprotonated (structures BPE-7^{TS} and BPE-11^{TS}) to give the observed condensation products (structures BPE-8 and BPE-12), completing the catalytic cycle.

The quantum chemical results discussed above were used in a microkinetic model as discussed in the previous section. To

DOI: 10.1021/acssuschemeng.5b00070
ACS Sustainable Chem. Eng. 2015, 3, 1339−1347

compare the model agreement with experimental data, some species' concentrations were summed. For this reaction, the experimentally observed concentration of BPE is compared to the sum of the predicted concentrations with the proton at and away from the ether oxygen (structures BPE-0 and BPE-1). To test the mechanism based only on its prediction of the observed products, only data points with less than 14% unaccounted for mass were used in the parameter optimization. Pre-exponential factors and activation energies derived from the quantum chemical calculations or the Smoluchowski equation, when appropriate, are summarized in Table 1.

Although the microkinetic model qualitatively captured the experimental data well, its quantitative agreement was improved by allowing two E_a values to be adjusted within typical uncertainty of quantum chemical calculations of ±3 kcal/mol based on an unweighted sum of squares as the objective function. The two E_a values that were optimized were for the nucleophilic attack (Figure 1, BPE-2^{TS}) and the formation of the protonated ortho condensation product (Figure 1, BPE-5^{TS}). The barrier to formation of the protonated para condensation product (Figure 1, BPE-9^{TS}) was optimized indirectly by parametrizing its activation energy in terms of the activation energy of BPE-5^{TS}. This was done to ensure an ortho/para ratio of 3.2, as seen experimentally and assumed to be constant, and to ensure that all optimized parameters were sensitive. By setting the ratio of the rate constants equal to this value, it was found that BPE-9^{TS} was reduced by 1.7 kcal/mol relative to BPE-5^{TS}. The optimized parameters involved a reduction in the barrier to nucleophilic attack of 1.8 kcal/mol and an increase in the barrier to formation of the ortho condensation product of 1.1 kcal/mol, leading to a final sum of squares value of 1.1×10^{-5}. The calculated concentration profiles for the disappearance of BPE and the formation of major products (phenol and benzyl alcohol) are compared to the experimental values in Figure 3 (Panel A, 130 °C; Panel B, 150 °C).

Model and experimental results for appearance of ortho and para condensation products are shown in Figure 4. In the 130 °C case (Panel A), although the modeled trend in appearance and ratio of ortho to para products is similar to the experimental data, the magnitudes of the concentrations differ by 1 order of magnitude. In the 150 °C case (Panel B), where mass is well conserved throughout, excellent reproduction of the total amount of condensation products is obtained. Note that in this case, the *y*-axes only differ by a factor of 2 rather than 1 order of magnitude.

Acidolysis of (1-Phenoxyethyl)benzene (PEB). The raw data for the acidolysis experiments on PEB are given in the Supporting Information. As shown in these data and in Figure 6 (Panel A, 130 °C; Panel B, 150 °C), the acidolysis of PEB proceeds much more rapidly than BPE. As before, the monoaromatic alcohols are the predominant species with the ratio of phenol and α-methyl-benzyl alcohol (AMBA) very near one to one.

Based on the accurate results obtained for BPE, the PEB system was also modeled with four explicit water molecules and a proton. The reaction coordinate leading to the formation of the major products of phenol and AMBA and condensation products is shown in Figure 5, and the three-dimensional structures are shown in SI-Figure 3 and SI-Figure 4 in the Supporting Information.

As evidenced by the experimental results, the PEB reaction is accelerated compared to BPE, and the quantum chemical

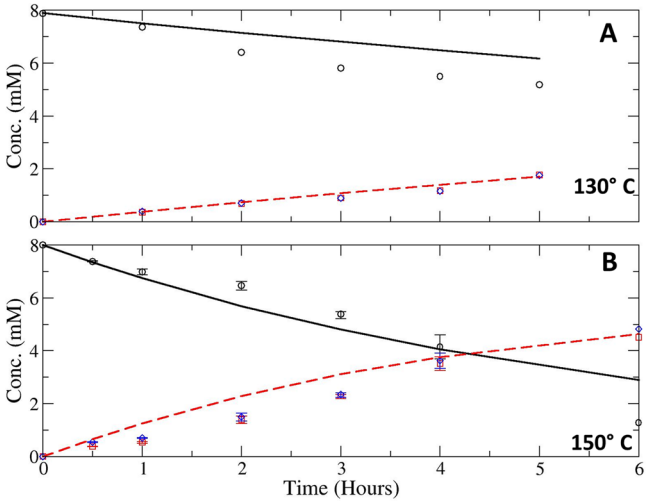

Figure 3. Comparison of optimized concentration profiles for BPE (solid black line for calculated, black circles for experimental result), major products (dashed red line for calculated, blue diamonds for the experimental phenol and red squares for the experimental benzylalcohol) at 130° (Panel A) and 150 °C (Panel B). Error analysis was only conducted for the 150 °C data. Only experimental time points with less than 14% unaccounted for mass were used for optimization and are shown here. See SI-Table 2 in the Supporting Information for details.

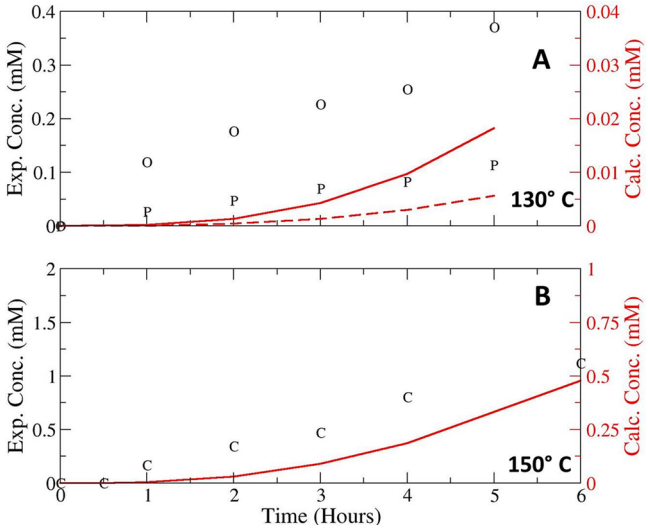

Figure 4. Concentration profiles for condensation products at 130° (Panel A) and 150 °C (Panel B). Experimental ortho and para concentrations in Panel A are shown with O and P, respectively, and are referenced to the *y*-axis on the left. Calculated concentration profiles are shown with solid red lines (ortho) and dashed red lines (para) and are referenced to the *y*-axis on the right. For the 150 °C study, only the total amount of condensation product was measured, not the separate ortho and para isomers. The total concentration of condensation products is indicated by the letter C. The calculated concentration is shown with a solid line and is referenced to the right *y*-axis.

calculations are able to capture this behavior as a lower barrier for nucleophilic attack. This difference between the propensities for the nucleophilic attack for the two different model compounds can be understood by referencing the calculated partial charges on the ether oxygen using the Natural Bond Orbital (NBO) method[63] and examining the localized

DOI: 10.1021/acssuschemeng.5b00070
ACS Sustainable Chem. Eng. 2015, 3, 1339−1347

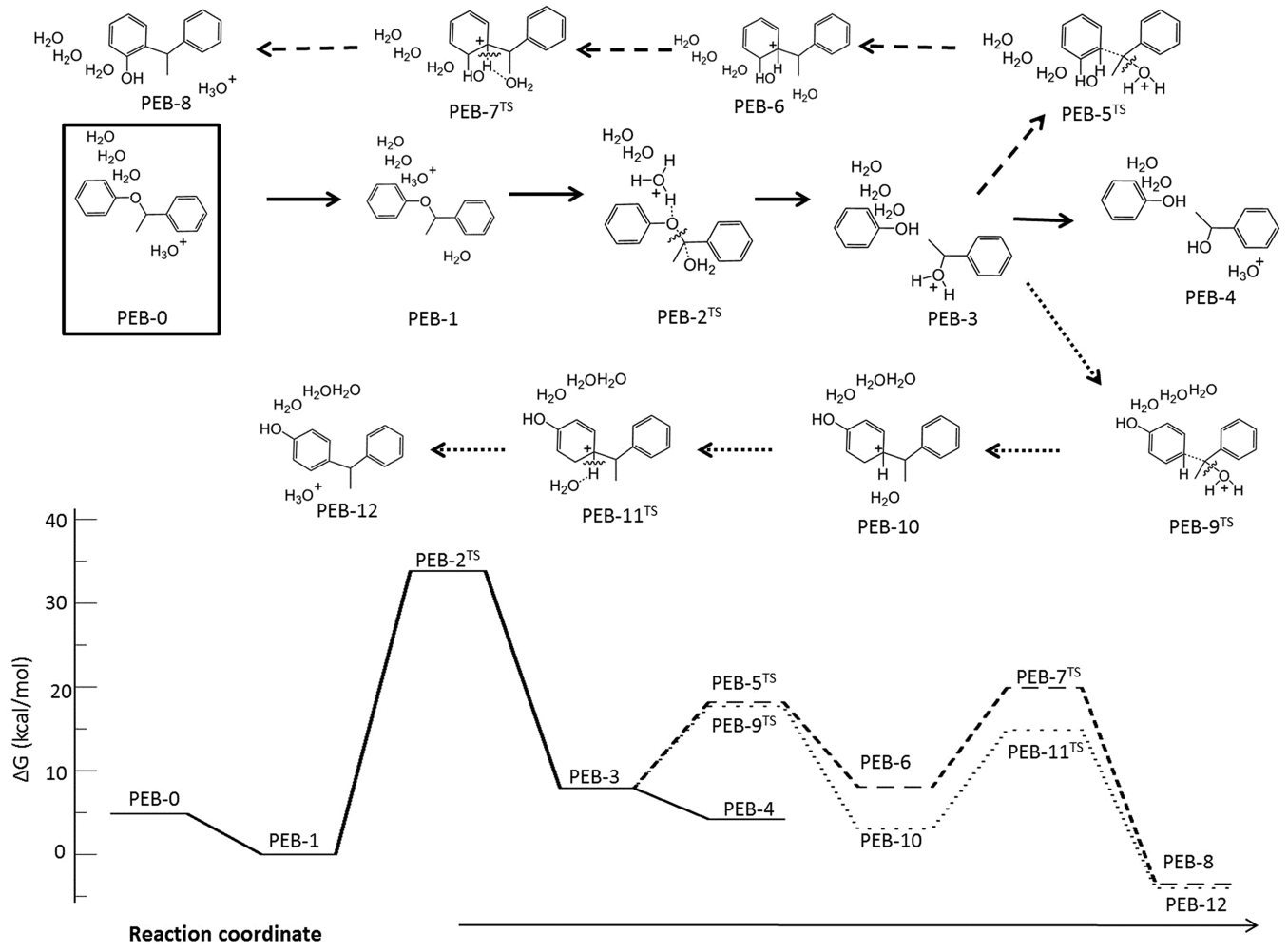

Figure 5. Reaction coordinate for the formation of the major products (solid line) along with the ortho (---) and para (···) condensation products for the PEB system. Note that the line scheme used in the plot is maintained in the arrow scheme between the corresponding structures. These arrows are only a guide for the eye. See the Supporting Information for corresponding three-dimensional structures.

Table 2. Natural Bond Orbital Method and Examination of the Localized Antibonding Orbital between the Ether Oxygen and the α-Carbon within the NBO Scheme[a]

	charge on ether oxygen (e^-)	scaled charges (% total e^-)	E (O_{ether}–C_α)* (au)	Occ. (O_{ether}–C_α)* (e^-)
phenol	−0.6946			
BPE-1	−0.61266		0.1914	0.0444
BPE-2^{TS}	−0.63653		0.0886	0.12367
change	−0.0209	25.7	0.1028	0.0792
PEB-1	−0.6198		0.1705	0.07538
PEB-2^{TS}	−0.6298		0.0769	0.13751
change	−0.0100	13.4	0.0936	0.06213

[a]The first column gives the calculated partial charges on the ether oxygen for the ground state structures (BPE and PEB), the transition state structures (BPE^{TS} and PEB^{TS}), and the final product (Phenol). The second column shows the percentage of the partial charge that must be transferred from the ground state structure to the final product that has already been transferred by the transition state. The final two columns give the energy and occupancy of the antibonding orbital of the localized bond between the ether oxygen and the α-carbon (see the Supporting Information).

antibonding orbital between the ether oxygen and the α-carbon within the NBO scheme (Table 2).

We examine the charge transfer at the transition state by comparing the partial charge difference on the ether oxygen in structure BPE-1 (PEB-1) and structure BPE-2^{TS} (PEB-2^{TS}) with the total amount of charge transfer that occurs between structure BPE-1 (PEB-1) and structure BPE-3 (PEB-3), wherein the ether oxygen becomes the phenolic oxygen. By scaling the amount of charge transferred at the transition state by the total that must be transferred to create the products, we can determine how much is transferred before the transition state and how much is transferred after. As shown in Table 2, in the case of the nucleophilic attack on PEB, only about 13% of the total charge that must be transferred in the course of the reaction occurs before the transition state, with 87% being transferred after. The value for BPE is higher by nearly a factor

DOI: 10.1021/acssuschemeng.5b00070
ACS Sustainable Chem. Eng. 2015, 3, 1339−1347

Table 3. Elementary Steps and Kinetic Parameters for PEB Microkinetic Model[a]

reaction	$A_{forward}$ (L/mol·s)	$E_{a\text{-}forward}$ (kcal/mol)	$A_{reverse}$ (L/mol·s)	$E_{a\text{-}reverse}$ (kcal/mol)
PEB-0 ⇆ PEB-1	5.2×10^{10}	0	9.1×10^{9}	2.2
PEB-1 ⇆ PEB-3	2.4×10^{7}	21.6 (**20.6 ± 0.095**)	1.4×10^{9}	21.9 (**20.9 ± 0.095**)
PEB-3 ⇆ PEB-4	5.2×10^{10}	0.0	1.6×10^{8}	1.1
PEB-3 ⇆ PEB-6	8.6×10^{8}	22.5	2.5×10^{10}	20.2
PEB-6 ⇆ PEB-8	2.2×10^{12}	10.7	7.6×10^{12}	23.3
PEB-3 ⇆ PEB-10	2.5×10^{9}	20.4	5.0×10^{10}	22.8
PEB-10 ⇆ PEB-12	1.8×10^{12}	10.5	2.2×10^{12}	17.8

[a]Values in bold indicate 95% probability intervals obtained through parameter optimization. See text for details.

of 2, explaining why the activation energy is significantly larger for this case. It is also instructive to examine the localized natural bonding orbital between the ether oxygen and the α-carbon. Relative to PEB, the energy of the antibonding orbital in BPE must be reduced by a larger amount to reach the transition state. Also, the occupancy of the antibonding orbital must change by a larger amount in order for the reaction to occur.

The DFT results discussed above for PEB were also incorporated into a microkinetic model, and the results were compared to experimental data. Parameter estimation was then carried out, allowing barriers of select reactions to be adjusted to obtain optimal agreement with experimental concentrations.

All kinetic parameters are summarized in Table 3, with values that were adjusted via parameter estimation shown in bold, using the experimental points with less than 14% mass loss for fitting. In this case, a reduction in the barrier to nucleophilic attack of only 1.0 kcal/mol (structure PEB-2^{TS}) was needed, giving a sum of squares value of 7.37×10^{-6}. The optimization was insensitive to any perturbations on the barriers to formation of condensation products. As in the case of BPE, this correction is well within the typical uncertainty for DFT calculations, suggesting that the kinetic model leading to the major products is reasonable.

The agreement between our calculated results and the measured values can are shown in Figure 6. In this case, the experimental mass balance is much better than for BPE. The model agrees very well over all times and temperatures for which the experimental mass balance was reasonable. Given that the model captured the two major products well, it was used to predict the concentrations of the two condensation products. The excellent mass balance closure in the experimental data even at high PEB conversion values suggested that the condensation products exhibit low yields at these time scales. The microkinetic model is in accord with these observations, predicting very low concentrations at all temperatures and time points.

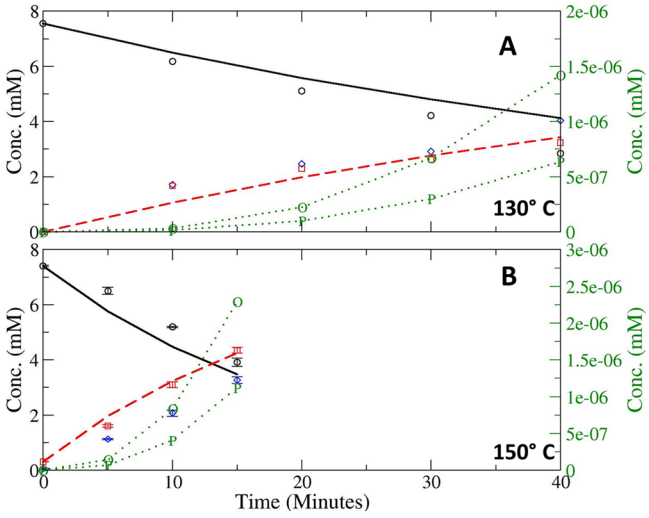

Figure 6. Concentration profiles for PEB acidolysis reaction at 130 °C (Panel A) and 150 °C (Panel B). The concentrations of PEB (solid black line for calculated, black circles for experimental result) and major products (red dashed for calculated, blue diamonds for the experimental phenol and red squares for the experimental AMBA) are referenced to the y-axis on the left. The total concentration of ortho and para condensation products predicted by the model are indicated with green O and P, respectively, with the dotted green line and are referenced to the right y-axis.

CONCLUSIONS

In this study, we sought to understand the major pathways of acid-catalyzed cleavage of the α-O-4 ether linkage of lignin. Two α-O-4 lignin model compounds were subjected to acid catalyzed cleavage in dilute acid at two temperatures similar to those used in dilute acid pretreatment. The rate of reaction was found to increase by an order of magnitude with methyl substitution at the α-carbon, implying the importance of substituent effects in the acidolysis of native lignin, similar in spirit to previous work for β-O-4 linkages, which demonstrated that a phenolic hydroxyl group greatly accelerates acid-catalyzed ether cleavage.[32] We used quantum chemical calculations and microkinetic modeling to evaluate a proposed mechanism for the reaction of these two compounds and found that the same mechanism, a nucleophilic attack of water on the α-carbon commensurate with protonation of the ether oxygen, gave excellent agreement with both sets of kinetic data. Condensation products were measured in addition to the major products for BPE and predicted by the microkinetic models for both BPE and PEB, and it was found that significant concentrations are only expected on the longer time scale observed in BPE. The formation of these products includes a much larger barrier for PEB relative to BPE, whereas the trend for the barrier to formation of the major product alcohols obeys the opposite trend. Therefore, on the times scales of the acidolysis of PEB substrate and collection of products, it is unlikely that significant concentrations of condensation products will accumulate. We expect similar results in cases of more highly substituted model compounds that incorporate the hydroxyl and methoxyl groups found in native lignin. These substituents have been found to greatly increase the rates of acidolysis in β-O-4 model compounds,[32] and the incorporation of electron donating groups into the phenyl rings is expected to have similar effects on the overall kinetics as the methylation of the α-carbon.

DOI: 10.1021/acssuschemeng.5b00070
ACS Sustainable Chem. Eng. 2015, 3, 1339−1347

■ ASSOCIATED CONTENT

Supporting Information

Details on how the DFT functional was chosen, raw data for acidolysis of BPE and PEB at 130 and 150 °C, data for error bars for 150 °C measurements for BPE and PEB, pictures and coordinates of all minima and transitions states of BPE and PEB shown in Figures 2 and 5, and a picture of the localized antibonding orbital between the ether oxygen and α-carbon for BPE. The Supporting Information is available free of charge on the ACS Publications website at DOI: 10.1021/acssuschemeng.5b00070.

■ AUTHOR INFORMATION

Corresponding Authors

*A. W. Pelzer. E-mail: adam.pelzer@northwestern.edu.
*L. J. Broadbelt. E-mail: broadbelt@northwestern.edu.
*G. T. Beckham. E-mail: gregg.beckham@nrel.gov.

Notes

The authors declare no competing financial interest.

■ ACKNOWLEDGMENTS

Work performed by A.W.P. was supported by the National Science Foundation under Grant No. CHE-1314063. We acknowledge funding from the National Advanced Biofuels Consortium, which was funded by the DOE BioEnergy Technologies Office through American Recovery and Reinvestment Act Funds. This research used resources of the National Energy Research Scientific Computing Center, a DOE Office of Science User Facility supported by the Office of Science of the U.S. Department of Energy under Contract No. DE-AC02-05CH11231. We also acknowledge support from the Department of Energy Grant No. DE-EE0005006 and Virent, Inc.

■ REFERENCES

(1) Chundawat, S. P.; Beckham, G. T.; Himmel, M. E.; Dale, B. E. Deconstruction of lignocellulosic biomass to fuels and chemicals. *Annu. Rev. Chem. Biomol. Eng.* **2011**, *2*, 121−145.

(2) Davda, R. R.; Shabaker, J. W.; Huber, G. W.; Cortright, R. D.; Dumesic, J. A. A review of catalytic issues and process conditions for renewable hydrogen and alkanes by aqueous-phase reforming of oxygenated hydrocarbons over supported metal catalysts. *Appl. Catal., B* **2005**, *56*, 171−186.

(3) Alonso, D. M.; Bond, J. Q.; Dumesic, J. A. Catalytic conversion of biomass to biofuels. *Green Chem.* **2010**, *12*, 1493−1513.

(4) Atsumi, S.; Liao, J. C. Metabolic engineering for advanced biofuels production from *Escherichia coli*. *Curr. Opin. Biotechnol.* **2008**, *19*, 414−419.

(5) Lee, S. Y.; Park, J. H.; Jang, S. H.; Nielsen, L. K.; Kim, J.; Jung, K. S. Fermentative butanol production by *Clostridia*. *Biotechnol. Bioeng.* **2008**, *101*, 209−228.

(6) Peralta-Yahya, P. P.; Zhang, F.; del Cardayre, S. B.; Keasling, J. D. Microbial engineering for the production of advanced biofuels. *Nature* **2012**, *488*, 320−328.

(7) Achyuthan, K. E.; Achyuthan, A. M.; Adams, P. D.; Dirk, S. M.; Harper, J. C.; Simmons, B. A.; Singh, A. K. Supramolecular self-assembled chaos: Polyphenolic lignin's barrier to cost-effective lignocellulosic biofuels. *Molecules* **2010**, *15*, 8641−8688.

(8) Chapple, C.; Ladisch, M.; Meilan, R. Loosening lignin's grip on biofuel production. *Nat. Biotechnol.* **2007**, *25*, 746−748.

(9) Ragauskas, A. J.; Beckham, G. T.; Biddy, M. J.; Chandra, R.; Chen, F.; Davis, M. F.; Davison, B. H.; Dixon, R. A.; Gilna, P.; Keller, M., et al. Lignin valorization: Improving lignin processing in the biorefinery. *Science* **2014**, *344*.

(10) Fu, C.; Mielenz, J. R.; Xiao, X.; Ge, Y.; Hamilton, C. Y.; Rodriguez, M.; Chen, F.; Foston, M.; Ragauskas, A.; Bouton, J.; et al. Genetic manipulation of lignin reduces recalcitrance and improves ethanol production from switchgrass. *Proc. Natl. Acad. Sci. U. S. A.* **2011**, *108*, 3803−3808.

(11) Bonawitz, N. D.; Kim, J. I.; Tobimatsu, Y.; Ciesielski, P. N.; Anderson, N. A.; Ximenes, E.; Maeda, J.; Ralph, J.; Donohoe, B. S.; Ladisch, M.; et al. Disruption of mediator rescues the stunted growth of a lignin-deficient *Arabidopsis* mutant. *Nature* **2014**, *509*, 376−380.

(12) Chen, F.; Dixon, R. A. Lignin modification improves fermentable sugar yields for biofuel production. *Nat. Biotechnol.* **2007**, *25*, 759−761.

(13) Lundquist, K. Acid degradation of lignin. Part 2: Separation and identification of low molecular weight phenols. *Acta Chem. Scand.* **1970**, *24*, 889−907.

(14) Linger, J. G.; Vardon, D. R.; Guarnieri, M. T.; Karp, E. M.; Hunsinger, G. B.; Franden, M. A.; Johnson, C. W.; Chupka, G.; Strathmann, T. J.; Pienkos, P. T. Lignin valorization through integrated biological funneling and chemical catalysis. *Proc. Natl. Acad. Sci. U. S. A.* **2014**, *111*, 12013−12018.

(15) Amen-Chen, C.; Pakdel, H.; Roy, C. Production of monomeric phenols by thermochemical conversion of biomass: A review. *Bioresour. Technol.* **2001**, *79*, 277−299.

(16) Zakzeski, J.; Bruijnincx, P. C. A.; Jongerius, A. L.; Weckhuysen, B. M. Valorization of lignin for the production of renewable chemicals. *Chem. Rev.* **2010**, *110*, 3552−3599.

(17) Lundquist, K.; Ericsson, L. Acid degradation of lignin. Part 3: Formation of formaldehyde. *Acta Chem. Scand.* **1970**, *24*, 3681−3685.

(18) Lundquist, K.; Lundgren, R. Acid degradation of lignin. Part 7: Cleavage of ether bonds. *Acta Chem. Scand.* **1972**, *26*, 2005−2023.

(19) Lundquist, K. Acid degradation of lignin. Part 8: Low molecular weight phenols from acidolysis of birch lignin. *Acta Chem. Scand.* **1973**, *27*, 2597−2606.

(20) Lundquist, K.; Hedlund, K. Acid degradation of lignin. Part 1: The formation of ketones of Hte guaiacylpropane series. *Acta Chem. Scand.* **1967**, *21*, 1750−1754.

(21) Agbor, V. B.; Cicek, N.; Sparling, R.; Berlin, A.; Levin, D. B. Biomass pretreatment: Fundamentals toward application. *Biotechnol. Adv.* **2011**, *29*, 675−685.

(22) Pepper, J. M.; Siddiqueullah, M. The effect of initial acid concentration on the lignin isolated by the acidolysis of aspen wood. *Can. J. Chem.* **1961**, *39*, 1454−1461.

(23) Pu, Y.; Hu, F.; Huang, F.; Davison, B. H.; Ragauskas, A. J. Assessing the molecular structure basis for biomass recalcitrance during dilute acid and hydrothermal pretreatments. *Biotechnol. Biofuels* **2013**, *6*, 15.

(24) Sarkanen, K. V.; Ludwig, C. H. *Lignins: Occurrence, Formation, Structure and Reactions*; Wiley-Interscience: New York, 1971.

(25) Feldman, D.; LaCasse, M.; Beznaczuk. Lignin-polymer systems and some applications. *Prog. Polym. Sci.* **1987**, *12*, 271−299.

(26) Grabber, J. H. How do lignin composition, structure, and cross-linking affect degradability? A review of cell wall model studies. *Crop Sci.* **2005**, *45*, 820−831.

(27) Heitner, C.; Dimmel, D.; Schmidt, J. A. *Lignin and Lignans Advances in Chemistry*; Taylor & Francis: Boca Raton, FL, 2010.

(28) Boerjan, W.; Ralph, J.; Baucher, M. Lignin biosynthesis. *Annu. Rev. Plant Biol.* **2003**, *54*, 519−546.

(29) Dolgonosov, B. M.; Gubernatorova, T. N. Modeling the biodegradation of multicomponent organic matter in an aquatic environment: 2. Analysis of the structural organization of lignin. *Water Resour.* **2010**, *37*, 320−331.

(30) Roberts, V.; Fendt, S.; Lemonidou, A. A.; Lercher, J. A. Influence of alkali carbonates on benzyl phenyl ether cleavage pathways in superheated water. *Appl. Catal., B* **2010**, *95*, 71−77.

(31) Beste, A.; Buchanan, A. C., III Computational investigation of the pyrolysis product selectivity for α-hydroxy phenethyl phenyl ether and phenethyl phenyl ether: Analysis of substituent effects and reactant conformer selection. *J. Phys. Chem. A* **2013**, *117*, 3235−3242.

(32) Sturgeon, M. R.; Kim, S.; Lawrence, K.; Paton, R. S.; Chmely, S. C.; Nimlos, M.; Foust, T. D.; Beckham, G. T. A mechanistic investigation of acid-catalyzed cleavage of aryl-ether linkages:

DOI: 10.1021/acssuschemeng.5b00070
ACS Sustainable Chem. Eng. 2015, 3, 1339−1347

Implications for lignin depolymerization in acidic environments. *ACS Sustainable Chem. Eng.* **2014**, *2*, 472−485.
(33) Grabow, L. C.; Gokhale, A. A.; Evans, S. T.; Dumesic, J. A.; Mavrikakis, M. Mechanism of the water gas shift reaction on Pt: First principles, experiments, and microkinetic modeling. *J. Phys. Chem. C* **2008**, *112*, 4608−4617.
(34) Bera, T.; Thybaut, J. W.; Marin, G. B. Single-event microkinetics of aromatics hydrogenation on Pt/H-ZSM22. *Ind. Eng. Chem. Res.* **2011**, *50*, 12933−12945.
(35) Nikbin, N.; Caratzoulas, S.; Vlachos, D. G. A first principles-based microkinetic model for the conversion of fructose to 5-hydroxymethylfurfural. *ChemCatChem* **2012**, *4*, 504−511.
(36) Craciun, I.; Reyniers, M.-F.; Marin, G. B. Liquid-phase alkylation of benzene with octenes over Y zeolites: Kinetic modeling including acidity descriptors. *J. Catal.* **2012**, *294*, 136−150.
(37) Ma, R.; Schuette, G. F.; Broadbelt, L. J. Insights into the relationship of catalytic activity and structure: A comparison study of three carbonic anhydrase mimics. *Int. J. Chem. Kinet.* **2014**, *46*, 683−700.
(38) Ma, R.; Schuette, G. F.; Broadbelt, L. J. Microkinetic modeling of CO_2 hydrolysis over Zn-(1,4,7,10-tetraazacyclododecane) catalyst based on first principles: Revelation of rate-determining step. *J. Catal.* **2014**, *317*, 176−184.
(39) Vinu, R.; Broadbelt, L. J. A mechanistic model of fast pyrolysis of glucose-based carbohydrates to predict bio-oil composition. *Energy Environ. Sci.* **2012**, *5*, 9808−9826.
(40) Bjorkman, K. R.; Schoenfeldt, N. J.; Notestein, J. M.; Broadbelt, L. J. Microkinetic modeling of *cis*-cyclooctene oxidation on heterogeneous Mn−tmtacn complexes. *J. Catal.* **2012**, *291*, 17−25.
(41) Mayes, H. B.; Broadbelt, L. J. Unraveling the reactions that unravel cellulose. *J. Phys. Chem. A* **2012**, *116*, 7098−7106.
(42) Mayes, H. B.; Tian, J.; Nolte, M. W.; Shanks, B. H.; Beckham, G. T.; Gnanakaran, S.; Broadbelt, L. J. Sodium ion interactions with aqueous glucose: Insights from quantum mechanics, molecular dynamics, and experiment. *J. Phys. Chem. B* **2013**, *118*, 1990−2000.
(43) Mayes, H. B.; Nolte, M. W.; Beckham, G. T.; Shanks, B. H.; Broadbelt, L. J. The alpha−bet(a) of glucose pyrolysis: Computational and experimental investigations of 5-hydroxymethylfurfural and levoglucosan formation reveal implications for cellulose pyrolysis. *ACS Sustainable Chem. Eng.* **2014**, *2*, 1461−1473.
(44) Zhou, X.; Nolte, M. W.; Mayes, H. B.; Shanks, B. H.; Broadbelt, L. J. Experimental and mechanistic modeling of fast pyrolysis of neat glucose-based carbohydrates. 1. Experiments and development of a detailed mechanistic model. *Ind. Eng. Chem. Res.* **2014**, *53*, 13274−13289.
(45) Zhou, X.; Nolte, M. W.; Shanks, B. H.; Broadbelt, L. J. Experimental and mechanistic modeling of fast pyrolysis of neat glucose-based carbohydrates. 2. Validation and evaluation of the mechanistic model. *Ind. Eng. Chem. Res.* **2014**, *53*, 13290−13301.
(46) Wu, X. Y.; Lü, X. Y. Hydrolysis kinetics of benzyl phenyl ether in high temperature liquid water. *Chin. Chem. Lett.* **2011**, *22*, 733−737.
(47) He, J.; Lu, L.; Zhao, C.; Mei, D.; Lercher, J. A. Mechanisms of catalytic cleavage of benzyl phenyl ether in aqueous and apolar phases. *J. Catal.* **2014**, *311*, 41−51.
(48) Siskin, M.; Brons, G.; Vaughn, S. N. Aqueous organic chemistry. 3. Aquathermolysis: Reactivity of ethers and esters. *Energy Fuels* **1990**, *4*, 488−492.
(49) Townsend, S. H.; Abraham, M. A.; Hupper, G. L.; Klein, M. T.; Paspek, S. C. Solvent effects during reactions in supercritical water. *Ind. Eng. Chem. Res.* **1988**, *27*, 143−149.
(50) Koyama, M. Hydrocracking of lignin-related model dimers. *Bioresour. Technol.* **1993**, *44*, 209−215.
(51) Mahdavi, B.; Lafrance, A.; Martel, A.; Lessard, J.; Menard, H. Electrocatalytic hydrogenolysis of lignin model dimers at Raney nickel electrodes. *J. Appl. Electrochem.* **1997**, *2*, 605−611.
(52) Lajunen, M.; Laine, R.; Aaltonen, M. Acid-catalyzed hydrolysis of some primary alkyl phenyl ethers. *Acta Chem. Scand.* **1997**, *51*, 1155−1161.
(53) Cox, R. A. Revised mechanism for the hydrolysis of ethers in aqueous acid1. *Can. J. Chem.* **2012**, *90*, 811−818.
(54) Cox, R. A.; Bunce, M. Three different mechanism for azo-ether hydrolyses in aqueous acid. *Can. J. Chem.* **2012**, *90*, 791−797.
(55) Cox, R. A. A greatly under-appreciated fundamental principle of physical organic chemistry. *Int. J. Mol. Sci.* **2011**, *12*, 8316−8332.
(56) Frisch, M. J.; Trucks, G. W.; Schlegel, H. B.; Scuseria, G. E.; Robb, M. A.; Cheeseman, J. R.; Scalmani, G.; Barone, V.; Mennucci, B.; Petersson, G. A.; Nakatsuji, H.; Caricato, M.; Li, X.; Hratchian, H. P.; Izmaylov, A. F.; Bloino, J.; Zheng, G.; Sonnenberg, J. L.; Hada, M.; Ehara, M.; Toyota, K.; Fukuda, R.; Hasegawa, J.; Ishida, M.; Nakajima, T.; Honda, Y.; Kitao, O.; Nakai, H.; Vreven, T.; Montgomery, J. A., Jr.; Peralta, P. E.; Ogliaro, F.; Bearpark, M.; Heyd, J. J.; Brothers, E.; Kudin, K. N.; Staroverov, V. N.; Kobayashi, R.; Normand, J.; Raghavachari, K.; Rendell, A.; Burant, J. C.; Iyengar, S. S.; Tomasi, J.; Cossi, M.; Rega, N.; Millam, N. J.; Klene, M.; Knox, J. E.; Cross, J. B.; Bakken, V.; Adamo, C.; Jaramillo, J.; Gomperts, R.; Stratmann, R. E.; Yazyev, O.; Austin, A. J.; Cammi, R.; Pomelli, C.; Ochterski, J. W.; Martin, R. L.; Morokuma, K.; Zakrzewski, V. G.; Voth, G. A.; Salvador, P.; Dannenberg, J. J.; Dapprich, S.; Daniels, A. D.; Farkas, Ö.; Ortiz, J. V.; Cioslowski, J.; Fox, D. J. *Gaussian 09*; Gaussian, Inc.: Wallingford, CT, 2009.
(57) Pliego, J. R.; Riveros, J. M. The cluster-continuum model for the calculation of the solvation free energy of ionic species. *J. Phys. Chem. A* **2001**, *105*, 7241−7247.
(58) Kelly, C. P.; Cramer, C. J.; Truhlar, D. G. Adding explicit solvent molecules to continuum solvent calculations for the calculation of aqueous acid dissociation constants. *J. Phys. Chem. A* **2006**, *110*, 2493−2499.
(59) Yamabe, S.; Kawagishi, N. A computational study on the relationship between formation and electrolytic dissociation of carbonic acid. *Theor. Chem. Acc.* **2011**, *130*, 909−918.
(60) Baker, J.; Pulay, P. Assessment of the Handy−Cohen optimized exchange density functional for organic reactions. *J. Chem. Phys.* **2002**, *117*, 1441.
(61) Eyring, H. The activated complex in chemical reactions. *J. Chem. Phys.* **1935**, *3*, 107.
(62) Calef, D. F.; Deutch, J. M. Diffusion-controlled reactions. *Annual Review Physical Chemistry* **1983**, *34*, 493−524.
(63) Weinhold, F. Natural Bond Orbital analysis: A critical overview of relationships to alternative bonding perspectives. *J. Comput. Chem.* **2012**, *33*, 2363−2379.

DOI: 10.1021/acssuschemeng.5b00070
ACS Sustainable Chem. Eng. 2015, 3, 1339−1347